Water and methanol in low-mass protostellar outflows: gas-phase synthesis, ice sputtering and destruction

Journal Item

Monthly Notices of the ROYAL ASTRONOMICAL SOCIETY

MNRAS **440,** 1844–1855 (2014) doi:10.1093/mnras/stu406
Advance Access publication 2014 March 27

Water and methanol in low-mass protostellar outflows: gas-phase synthesis, ice sputtering and destruction

A. N. Suutarinen,[1]★ L. E. Kristensen,[2] J. C. Mottram,[3] H. J. Fraser[1] and E. F. van Dishoeck[3,4]

[1]*Department of Physical Sciences, The Open University, Milton Keynes MK7 6AA, UK*
[2]*Harvard–Smithsonian Center for Astrophysics, 60 Garden Street, Cambridge, MA 02138, USA*
[3]*Leiden Observatory, Leiden University, PO Box 9513, NL-2300 RA Leiden, the Netherlands*
[4]*Max-Planck-Institut für Extraterrestrische Physik, Giessenbachstrasse 1, D-85748 Garching, Germany*

Accepted 2014 February 27. Received 2014 February 27; in original form 2013 December 19

ABSTRACT

Water in outflows from protostars originates either as a result of gas-phase synthesis from atomic oxygen at $T \gtrsim 200$ K, or from sputtered ice mantles containing water ice. We aim to quantify the contribution of the two mechanisms that lead to water in outflows, by comparing observations of gas-phase water to methanol (a grain surface product) towards three low-mass protostars in NGC 1333. In doing so, we also quantify the amount of methanol destroyed in outflows. To do this, we make use of James Clerk Maxwell Telescope and *Herschel*-Heterodyne Instrument for the Far-Infrared data of H_2O, CH_3OH and CO emission lines and compare them to RADEX non-local thermodynamic equilibrium excitation simulations. We find up to one order of magnitude decrease in the column density ratio of CH_3OH over H_2O as the velocity increases in the line wings up to $\sim$15 km s^{-1}. An independent decrease in $X(CH_3OH)$ with respect to CO of up to one order of magnitude is also found in these objects. We conclude that gas-phase formation of H_2O must be active at high velocities (above 10 km s^{-1} relative to the source velocity) to re-form the water destroyed during sputtering. In addition, the transition from sputtered water at low velocities to form water at high velocities must be gradual. We place an upper limit of two orders of magnitude on the destruction of methanol by sputtering effects.

Key words: astrochemistry – stars: formation – ISM: jets and outflows – ISM: molecules.

1 INTRODUCTION

Water plays a unique role in probing the physical and chemical conditions of star-forming regions. In the cold regions of protostars, water is frozen out as ice covering the dust grains, with only trace amounts found in the gas phase ($\lesssim 10^{-7}$; Caselli et al. 2012; Herpin et al. 2012; Mottram et al. 2013; Schmalzl et al., in preparation). The molecular outflows launched by the accreting protostar form an interesting laboratory for studying water in protostellar systems: the high water abundances observed in outflows ($>10^{-6}$; Nisini et al. 2010; Bjerkeli et al. 2012; Santangelo et al. 2012; Vasta et al. 2012; Dionatos et al. 2013; Van Loo et al. 2013) arise from a combination of sputtering of ice mantles and direct gas-phase synthesis; however, the relative water abundance contributions are unknown. Constraining the relative contributions of these two routes is important for using water as a diagnostic of the physical conditions in outflows, as well as constraining the chemistry in the various parts of the outflow.

Water formation on dust grains is a complicated process (e.g. Ioppolo et al. 2008; Lamberts et al. 2013), but generally involves the repeated hydrogenation of oxygen-bearing species such as O, OH and O_2 (Tielens & Hagen 1982). The only efficient gas-phase formation route for H_2O is a high-temperature ($T \gtrsim 200$ K) neutral–neutral reaction chain (e.g. Draine, Roberge & Dalgarno 1983; Bergin, Neufeld & Melnick 1999; Tielens 2005; Glassgold, Meijerink & Najita 2009):

$$\mathrm{O} \xrightarrow{\mathrm{H_2}} \mathrm{OH} \xrightarrow{\mathrm{H_2}} \mathrm{H_2O} + \mathrm{H}. \quad (1)$$

Another common grain surface material, methanol, can be formed on dust grains through repeated hydrogenation of CO (e.g. Tielens & Hagen 1982; Tielens 2005) as

$$\mathrm{CO_{surface}} \xrightarrow{\mathrm{H}} \mathrm{HCO_{surface}} \xrightarrow{\mathrm{H}} \mathrm{CH_3O_{surface}} \xrightarrow{\mathrm{H}} \mathrm{CH_3OH_{surface}}. \quad (2)$$

Unlike water, gas-phase reactions that produce CH_3OH are very slow compared to grain surface chemistry for any physical conditions expected within protostellar systems (Geppert et al. 2006).

Both water (e.g. Codella et al. 2010; van Dishoeck et al. 2011) and methanol (e.g. Bachiller et al. 1995; Kristensen et al. 2010a)

★E-mail: aleksi.suutarinen@iki.fi

have been detected in the gas phase of the outflows and shocks of young stellar objects (YSOs). In astrophysical environments, the grain surface reaction chain leads to grain surface abundances of the order of 10^{-6}–10^{-5} for CH_3OH with respect to gas-phase H_2 (e.g. van der Tak, van Dishoeck & Caselli 2000; Cuppen et al. 2009). This results in relative abundances of CH_3OH ice with respect to H_2O ice ranging from a few to ∼30 per cent (e.g. Dartois et al. 1999; Pontoppidan et al. 2003; Gibb et al. 2004; Pontoppidan, van Dishoeck & Dartois 2004; Boogert et al. 2008; Öberg et al. 2011). Models of cold dense clouds by Lee, Bettens & Herbst (1996), which only include gas-phase production, result in gas-phase abundances of CH_3OH no higher than between 10^{-10} and 10^{-9} on time-scales of up to 10^6 yr (Garrod et al. 2006; Geppert et al. 2006).

In the context of YSOs and their outflows, we assume and expect all of the grain surface formation of H_2O and CH_3OH to have already taken place during the preceding dark-cloud and pre-stellar core phases. Material is liberated from the grain surfaces either through thermal desorption if the temperature of the dust grains rises above ∼100 K for water (Fraser et al. 2001; Brown & Bolina 2007) and ∼85 K for methanol (Brown & Bolina 2007) as they journey close to the protostar (Visser et al. 2009), or through sputtering in shocks. While photodesorption due to cosmic ray-induced UV radiation is expected to be important in the cold conditions found in protostellar envelopes (e.g. Caselli et al. 2012; Mottram et al. 2013, Schmalzl et al. in preparation), it is unlikely to be dominant in the conditions found in outflows.

Therefore, any gas-phase CH_3OH observed in outflows will originate from sputtered ice mantle material, while gas-phase H_2O may originate either in warm shocked gas in outflows where the temperature exceeds ∼200 K (Bergin et al. 1999; Charnley 1999) or from the grain mantles. The first objective of this study is to test whether there is observational evidence in outflow material for water formation in excess of what we would expect to see from only ice mantle desorption, i.e. is the gas-phase formation route activated?

Our method for studying this is to examine the relative gas-phase column density variations of CH_3OH and H_2O derived in components of their emission spectra associated with the outflow and its shocked cavities, as seen towards the source positions of three prototypical YSOs. CH_3OH is a particularly good molecule for comparing against H_2O as it is a pure grain mantle species. Thus, any variations of $N(CH_3OH)/N(H_2O)$ are a result of independent variations in either $N(CH_3OH)$ or $N(H_2O)$.

Before we can use $N(CH_3OH)/N(H_2O)$ in studying the variations of $N(H_2O)$, we must first consider whether any CH_3OH is destroyed, either by dissociative desorption during sputtering or in the shock through reactions with H. This latter scenario would be somewhat similar to that involving another grain surface product, NH_3, at positions offset from the YSO (Codella et al. 2010; Viti et al. 2011). The second objective of this paper is to provide observational limits on the extent of CH_3OH destruction in the outflows of low-mass YSOs. This is accomplished by comparing the column densities to that of a CO line which traces the same gas as H_2O, such as CO $J = 10$–9 (Nisini et al. 2013; Santangelo et al. 2013; Tafalla et al. 2013; Yıldız et al. 2013). The $N(CH_3OH)/N(CO)$ ratio can then be translated into the CH_3OH abundance $X(CH_3OH) = N(CH_3OH)/N(H_2)$ by assuming a constant CO abundance in the outflow, 10^{-4}.

This paper is structured as follows. In Section 2, we describe our observations and then describe the immediate results in Section 3. In Section 4, we describe the decomposition of the acquired spectra into components, and explain which of these we assume to have the same physical origin. We also discuss the likely physical conditions in the outflow, and use them to constrain the radiative transfer simulations which allow us to convert our observed line intensity ratios into column density ratios. In Section 5, we discuss the acquired column density ratios and place them in the context of the arguments and processes outlined above. Finally, in Section 6, we summarize our results and draw our conclusions.

Table 1. Observed line parameters.

Line	Rest freq.[a] (GHz)	θ_{MB} ($''$)	E_{up}/k_b (K)	n^b_{crit} (cm^{-3})
H_2O $2_{02}-1_{11}$	987.927	21[c]	100.8	8×10^7
CH_3OH 5_K-4_K	241–242	21	41–136	5×10^5
CH_3OH 7_K-6_K	338–339	14	65–256	1×10^6
CO 10–9	1151.985	18[c]	304.2	5×10^5

[a]Pickett et al. (1998).
[b]Critical density at 200 K; for the CH_3OH transitions, the values reported are for the highest S/N K=0 A transitions.
[c]Calculated using equation 3 from Roelfsema et al. (2011).

2 OBSERVATIONS

The data used in this paper consist of spectroscopic observations of H_2O, CH_3OH and CO towards three Class 0 protostars: NGC 1333 IRAS 2A, 4A and 4B. The details of this sample are given in Table 2. Observations of the $2_{02}-1_{11}$ para-H_2O and CO $J = 10$–9 transitions were obtained with the Heterodyne Instrument for the Far-Infrared (HIFI; de Graauw et al. 2010) on the *Herschel* Space Observatory (Pilbratt et al. 2010) as part of the 'Water in star-forming regions with *Herschel*' key programme (WISH; van Dishoeck et al. 2011). The reduction of these data is discussed further in Kristensen et al. (2010a) and Yıldız et al. (2013), respectively. The J=5–4 and 7–6 K-ladders of CH_3OH were observed with the James Clerk Maxwell Telescope[1] (JCMT) with the RxA and RxB receivers, respectively. Details can be found in Maret et al. (2005). A summary of the frequencies, beam sizes and upper level energies (E_{up}) can be found in Table 1. A linear baseline was subtracted from all spectra, which were then placed on a common velocity scale, centred at the local rest velocity of the source. As the A-CH_3OH 7_0-6_0 data were obtained in a smaller beam than the other transitions, the line intensity was scaled down by a factor of ∼1.3–1.5 to take the difference in beam size into account (see Appendix A for further details).

The uncertainties reported in the rest of this paper only relate to the intrinsic random noise in each spectrum. Typical σ_{RMS} levels (in channel sizes binned to 1 km s^{-1}; see below) for the H_2O, CO and two CH_3OH lines are 0.02, 0.17, 0.15 and 0.24 K, respectively. The calibration uncertainty of the HIFI spectra is $\lesssim$10 per cent (Roelfsema et al. 2011) and the calibration uncertainty of the JCMT spectra is ∼20 per cent.

In the upcoming sections, when discussing the intensity ratios of the various lines included in this study, they have been resampled to fit a common velocity resolution of 1 km s^{-1} which was found to give a good balance between resolution and signal-to-noise ratio (S/N). Resampling also improves the S/N of the line wings, which are crucial for this study.

[1] The James Clerk Maxwell Telescope is operated by the Joint Astronomy Centre on behalf of the Science and Technology Facilities Council of the United Kingdom, the National Research Council of Canada and (until 2013 March 31) the Netherlands Organization for Scientific Research.

3 RESULTS

3.1 Line profiles

Fig. 1 shows the H_2O spectra of IRAS 2A, IRAS 4A and IRAS 4B at the source position, overlaid with both of the CH_3OH and CO spectra. For the wings of IRAS 2A, all profiles are very similar, although the red wing of the H_2O spectrum extends to higher velocities than any of the other species by about 5 km s^{-1}. IRAS 4A is characterized by the highly asymmetric profile of the CH_3OH 7–6 spectrum compared to the H_2O and CO 10−9 spectra. The H_2O line wings towards both IRAS 4A and 4B extend to significantly higher velocities than the CH_3OH and CO line wings by more than 10 km s^{-1}.

Previous studies have found that the observed H_2O line profiles are generally complex and consist of multiple dynamic components (Kristensen et al. 2010b, 2011, 2012, 2013; Mottram et al. 2013). These components are typically associated with the envelope, outflowing and shocked gas and trace physical components not detected previously. CH_3OH profiles, on the other hand, typically consist of just two components: one associated with the outflow and one with the envelope. In the following, we limit ourselves to studying the line wings only, and ignore the line centres which are typically associated with envelope emission.

The velocity ranges used as the red and blue wings of the objects are indicated by the, respectively, coloured bars at the top of Fig. 1. The ranges were selected such that any envelope contribution is excluded (typically ±2 km s^{-1} from the source velocity) and such that the line wings are completely included. Towards IRAS 4A and 4B, the redshifted A-CH_3OH 5_0-4_0 wing emission starts to blend with E-CH_3OH $5_{-1}-4_{-1}$ emission at velocities of +5–10 km s^{-1} from the source velocity, which therefore sets the upper limit on the redshifted velocity.

3.2 Observed line ratios

The line ratios of the two ground-state 5–4 and 7–6 A-CH_3OH transitions with respect to H_2O $2_{02}-1_{11}$ and CO 10–9 are presented in Fig. 2. The line ratios are measured where $\Delta v \geq 3$ km s^{-1}

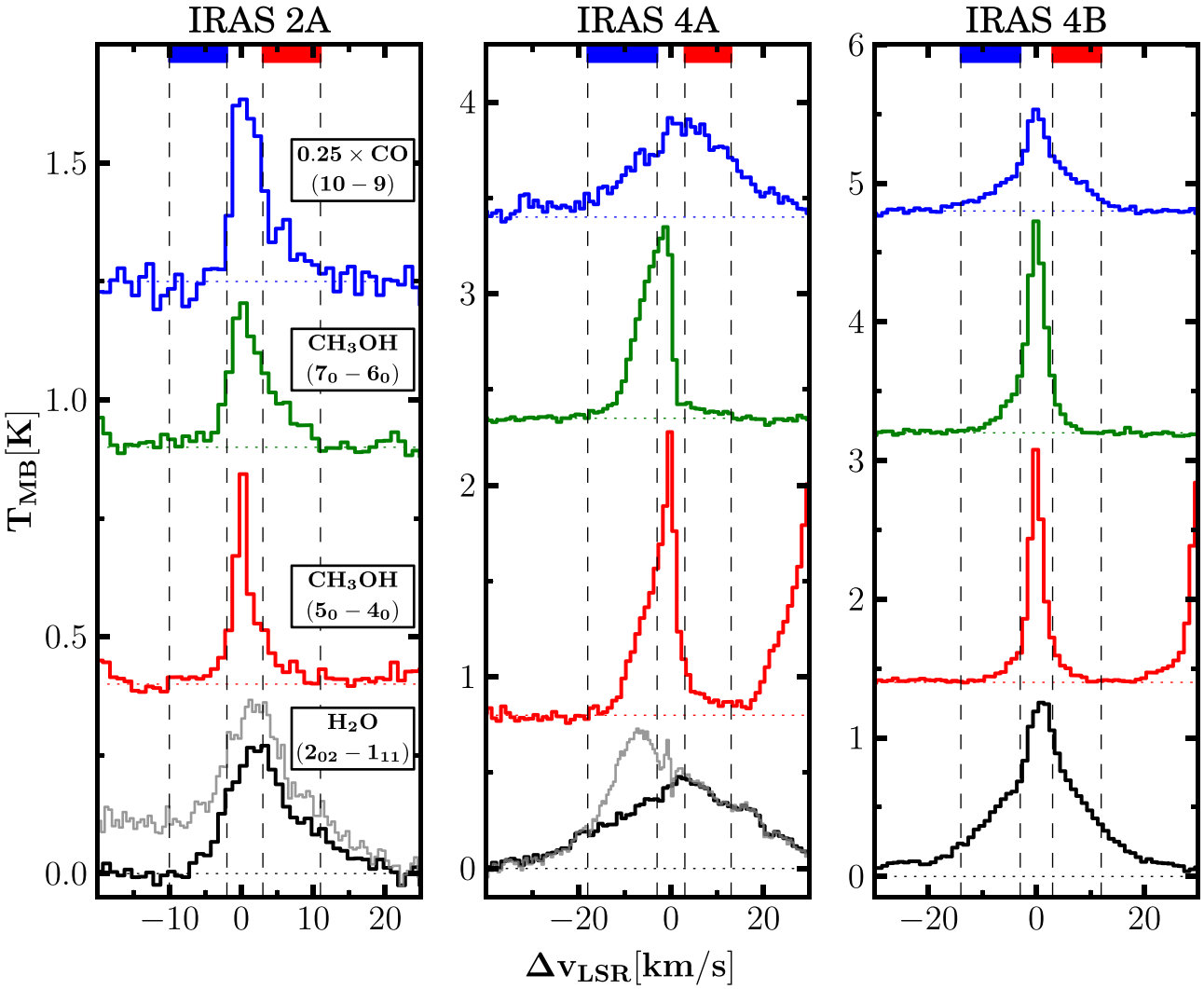

Figure 1. The emission of the 5_0-4_0 (red) and 7_0-6_0 (green) A-CH_3OH, the 10–9 (blue) CO spectra plotted above the $2_{02}-1_{11}$ p-H_2O spectrum (grey), which has been decomposed in the manner discussed in Section 5.1; decomposed spectra are shown in black. All spectra have been resampled to a common channel size of 1 km s^{-1}, and shifted to 0 km s^{-1}. The CO 10–9 spectrum has been scaled by 0.25. The spectra are offset along the *y*-axis for clarity. The dashed vertical lines show the velocity ranges used for selecting the red and blue wings of the spectra, as colour coded by the horizontal lines at the top.

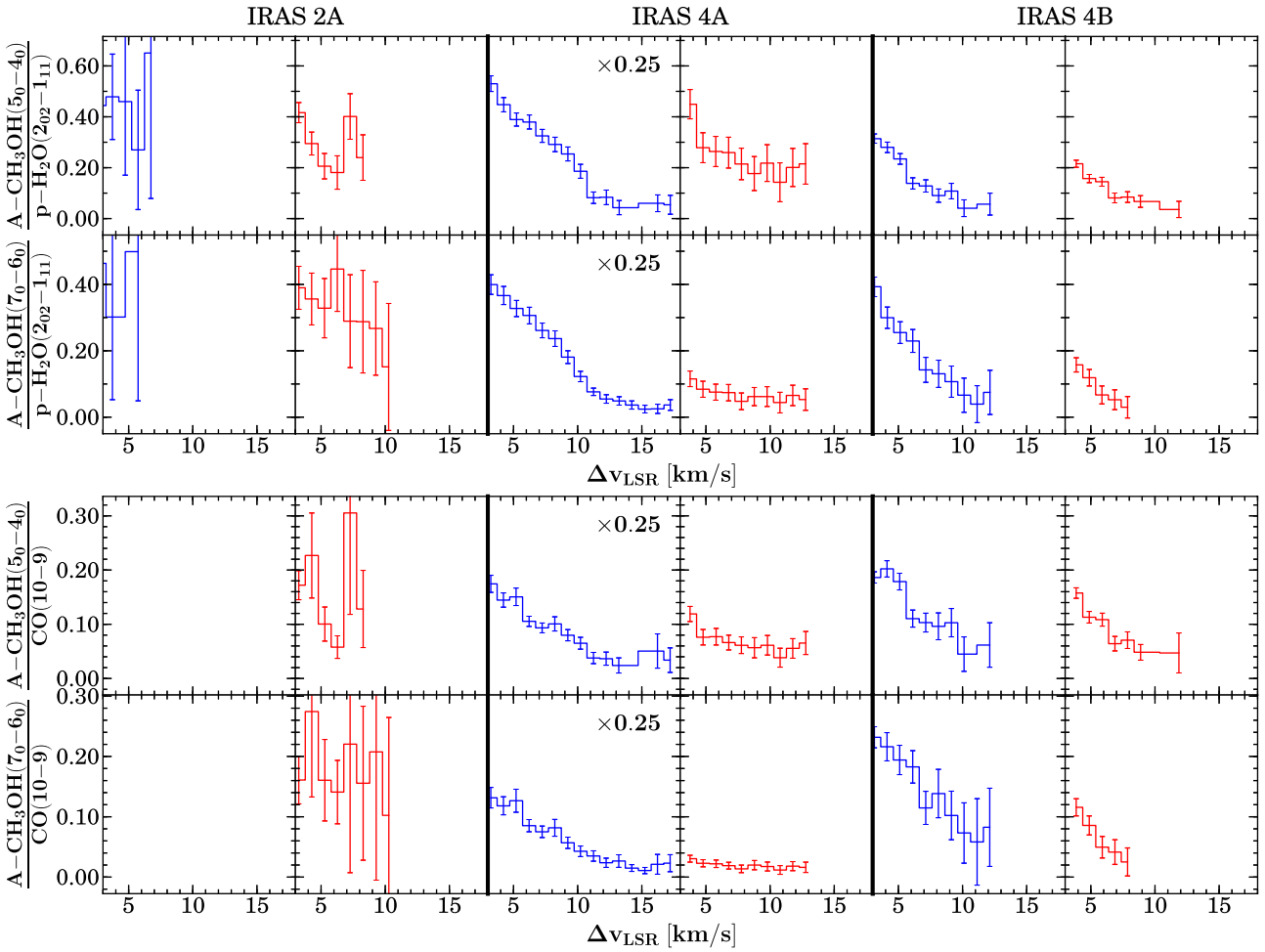

Figure 2. The ratio of the line intensities of two different A-CH_3OH lines (5_0-4_0 and 7_0-6_0 over the line intensity of the $2_{02}-1_{11}$ p-H_2O transition (top), CO 10−9 (bottom). The velocity along the *x*-axis is absolute offset with respect to the source velocity for the blue and red wings, respectively. Only the velocity range covering the line wings tracing emission related to the outflows is included in the line ratios and all points where S/N < 1 for either line have been ignored. Some of the line ratios were scaled for visibility reasons (marked). The error bars only include measurement uncertainties and not relative calibration uncertainties.

(at lower velocities, we cannot separate outflow emission from quiescent envelope emission) and S/N is >1 in both transitions. The CO 10–9 line profile towards IRAS 2A shows no blueshifted emission in spite of the high quality of the data.

The CH_3OH/H_2O line ratios show a decreasing trend with increasing velocity over the range where CH_3OH is detected. This is particularly visible towards IRAS 4A in the blue wing, where the ratio decreases by more than a factor of 5. Most other line wings show a decrease of a factor of 2–3. Only the IRAS 2A line wings appear to exhibit constant line ratios, although the higher S/N red 7_0-6_0 CH_3OH line wing shows a significant decrease with respect to H_2O emission. The CH_3OH/CO 10–9 line ratios (Fig. 2) exhibit similar trends as the ratios with H_2O, consistent with the similarity of the H_2O and CO 10–9 profiles (Yıldız et al. 2013).

4 ANALYSIS

4.1 RADEX and the degeneracy of the parameter space

The non-local thermodynamic equilibrium (LTE) excitation and radiative transfer software RADEX (van der Tak et al. 2007) is used to simulate the physical conditions of a body of gas in order to convert integrated molecular line intensities into corresponding column densities. The free parameters are the gas density ($n(H_2)$), temperature (T) and either the molecular column density (N) or the opacity (τ), given a line width Δv. RADEX relies on the escape probability approximation and assumes a slab geometry. In all following simulations except those used for generating Fig. 3 (where line width is used to control τ), we set the line width to 1 km s^{-1}, corresponding to the channel width. In the following, we assume that the H_2O o/p ratio is 3.0 (Emprechtinger et al. 2013). All column densities involving H_2O presented for the rest of the paper have made use of this ratio to convert N(p-H_2O) to $N(H_2O)$. The molecular line information RADEX uses is taken from LAMDA, (Schöier et al. 2005) with information for the individual molecules from Rabli & Flower (2010), Yang et al. (2010) and Daniel, Dubernet & Grosjean (2011).

Constraints must be placed on the parameter space if we are to obtain a non-degenerate solution to our data analysis. Since we are only interested in the relative abundance variations of CH_3OH, CO and H_2O, the line intensity ratios must be converted to column density ratios. In the following subsections we discuss what constraints can be put on the gas density, temperature and opacity based on relevant envelope and outflow parameters, and what the effect of varying these parameters is on the final column density ratio.

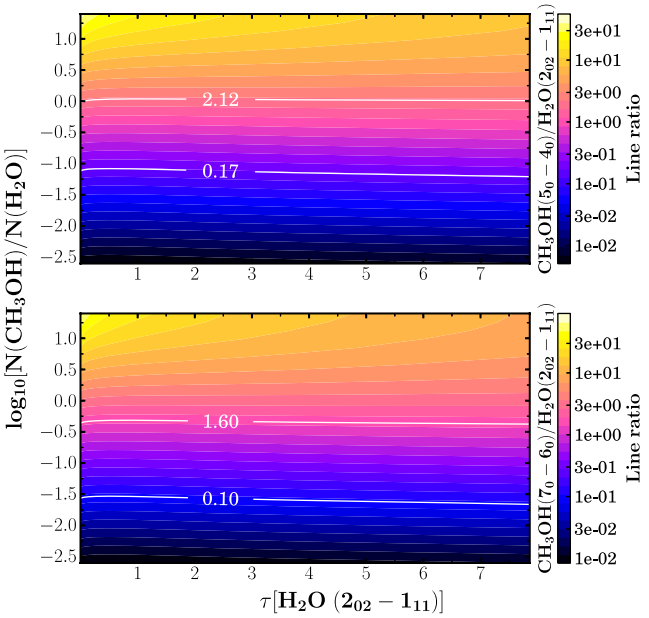

Figure 3. A visualization of RADEX simulations which show how the conversion of line intensity ratio to column density ratio behaves as a function of the optical depth of the H_2O emission in the case of CH_3OH versus H_2O, for two different CH_3OH transitions. The white contour lines show the maximum and minimum line intensity ratios of the blue wing of IRAS 4A. T_{kin} is fixed at 200 K, and $n(H_2)$ is fixed to be 10^6 cm^{-3}.

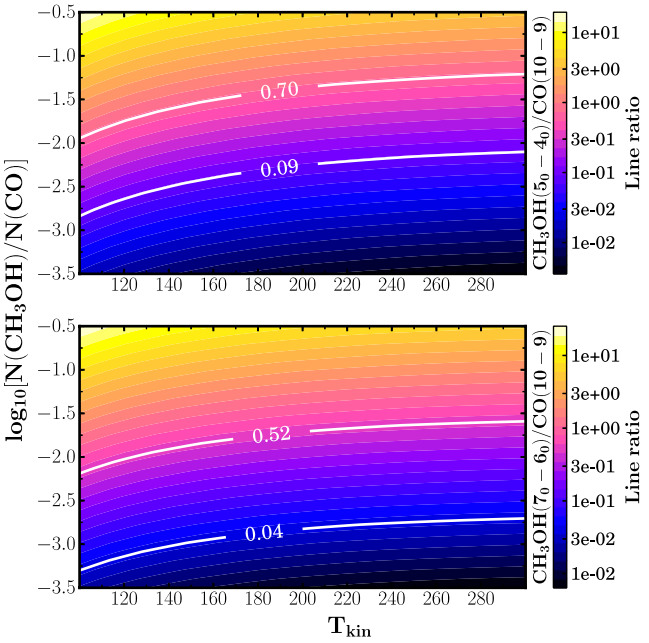

Figure 4. The effects of varying T_{kin} on the derived $N(CH_3OH)/N(CO)$ ratio in the optically thin limit for $n(H_2) = 10^6$ cm^{-3}, for two different CH_3OH transitions. The white contour lines show the maximum and minimum observed line intensity ratios for the blue wing of IRAS 4A, as shown in Fig. 2.

4.1.1 *Opacity and column density*

From Yıldız et al. (2013), we know that the CO 10–9 line wings are optically thin. For CH_3OH, observations towards pure outflow positions, such as L1157 B1 and B2 (Bachiller et al. 1995), result in inferred column densities in the line wings that suggest they are optically thin. We assume that this is true towards the protostellar position as well.

Water emission is known to be optically thick towards the protostellar position (Kristensen et al. 2011) with opacities >10 for the ground-state 557 GHz $1_{10}-1_{01}$ transition. However, because of the high critical density of water (>10^8 cm^{-3} for the 987 GHz transition studied here) compared to the H_2 density, the effective critical density is $A/(C\tau)$, where A is the Einstein A coefficient, C is the collisional rate coefficient and τ is the opacity. In the limit where the opacity is high but $n < n_{crit}$, the emission becomes effectively thin and a photon is lost for each radiative decay (Snell et al. 2000), i.e. while the emission may be optically thick, it is effectively optically thin.

A grid of RADEX simulations was run to study how increasing opacity affects the conversion of the observed line intensity ratios into column density ratios (Fig. 3). As can be seen, the effects of varying the opacity are limited much less than a factor of 2. The reason is that although the water emission is optically thick, it is effectively thin (see above). In the following, we therefore assume that the water emission is optically thin.

An additional constraint can be put on the CH_3OH/H_2O column density ratio. If the relative gas-phase abundance of CH_3OH and H_2O trace the relative ice-phase abundance of the same molecules, values are expected to range from a few to 30 per cent (e.g. Dartois et al. 1999; Pontoppidan et al. 2003, 2004; Gibb et al. 2004; Boogert et al. 2008; Öberg et al. 2011). Should gas-phase water formation be taking place, the gas-phase abundance ratio would be lower than the ice-phase abundance ratio, and $[N(CH_3OH)/N(H_2O)]_{gas} < [N(CH_3OH)/N(H_2O)]_{ice}$. Using $T_{kin} = 200$ K and $n(H_2) = 10^6$ cm^{-3} ensures that the inferred $N(CH_3OH) < N(H_2O)$ is always true for our data, even with optical depth effects accounted for.

4.1.2 *Temperature*

Examining the rotational temperatures (presented separately in Appendix B) of CH_3OH towards our objects places them above 'normal' cloud temperatures of 10–15 K but below outflow temperatures of 100−300 K. Though CH_3OH is not necessarily in LTE, it is not far off and we proceed with assuming that LTE applies for the CH_3OH lines, i.e. that $T_{kin} = T_{rot}$. The kinetic temperature range used in the RADEX simulations is 100–300 K, based on the universal warm temperature component seen in CO rotational diagrams of low-mass protostars (Herczeg et al. 2012; Green et al. 2013; Karska et al. 2013; Manoj et al. 2013).

Fig. 4 shows that the inferred CH_3OH/CO column density ratio increases by a factor of ∼3 from 100 to 300 K for a constant density of 10^6 cm^{-3}. The CH_3OH/H_2O column density ratio (Fig. 5) shows similar behaviour.

4.1.3 *Density*

One way of obtaining estimates of $n(H_2)$ is to use the envelope density at a given distance from the protostar for the outflow material (e.g. Kristensen et al. 2012; Yıldız et al. 2013). Kristensen et al. (2012) estimated the envelope density as a function of distance for all sources in this sample based on fits to the continuum spectral energy distribution and submm continuum maps, assuming a power-law density structure. Densities of ∼5 × 10^6 cm^{-3} are found at a distance of 1000 au, corresponding to ∼4 arcsec or half the beam radius. At the edge of the beam (10 arcsec, 2350 au), the density

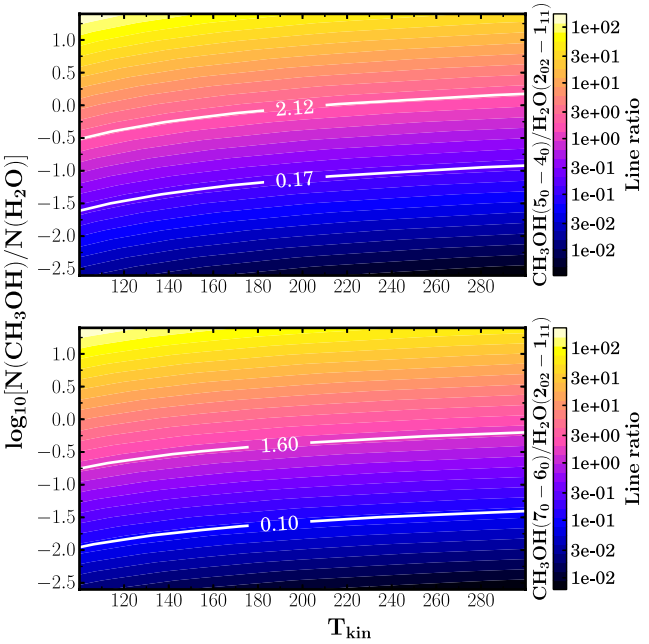

Figure 5. The effects of varying T_{kin} on the derived $N(CH_3OH)/N(H_2O)$ ratio in the optically thin limit, for $n(H_2) = 10^6$ cm^{-3}, for two different CH_3OH transitions. The white contour lines show the maximum and minimum observed line intensity ratios for the blue wing of IRAS 4A, as shown in Fig. 2.

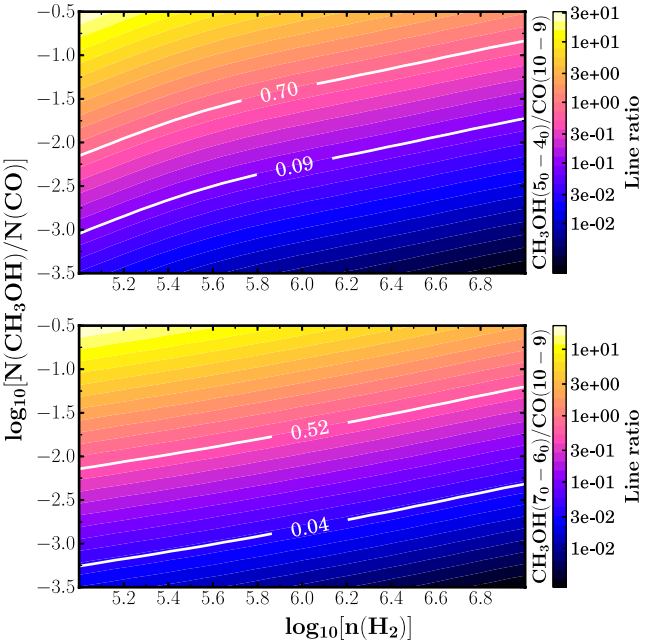

Figure 6. The simulated intensity ratio of CH_3OH 5_0-4_0 (top) and 7_0-6_0 (bottom) to CO 10–9 as contours of $\log_{10}(n(H_2))$ (*x*-axis) and $\log_{10}(N(CH_3OH)/N(CO))$ (*y*-axis). The white contour lines show the maximum and minimum observed line intensity ratios for the blue wing of IRAS 4A, as shown in Fig. 2. The contour levels are logarithmically scaled. The kinetic temperature is fixed at 200 K and all lines are optically thin.

is typically 10^6 cm^{-3}. Since the entrained gas in the outflow cavity walls can be either compressed by the shocks or expanding into the outflow cavity, we study $n(H_2)$ in the range of 10^5-10^7 cm^{-3}.

For comparison, the critical densities are listed in Table 2. The envelope densities exceed the CH_3OH and CO critical densities, whereas the H_2O critical density is never reached. Thus, the CH_3OH and CO level populations are likely thermally excited, whereas H_2O is subthermally excited. For CO and H_2O, this has been shown to be the case by Herczeg et al. (2012) using excitation analysis of *Herschel*-Photodetector Array Camera & Spectrometer (PACS) observations.

The effect the density range has on the line intensity ratio to column density ratio translation can be examined by running a grid of RADEX simulations in which τ and T_{kin} are kept constant (optically thin and 200 K, respectively) and $n(H_2)$ and the column density ratio are varied in order to produce line intensity ratios comparable to the observations. As both the CH_3OH and CO 10–9 line wings are optically thin (Yıldız et al. 2013, for CO), they form a good benchmark for exploring the effects of the physical environment on the simulated line ratios while allowing us to ignore τ. The results of the RADEX simulation grid are shown as a contour plot in Fig. 6, where they are compared with the observed ratios for the blue wing of IRAS 4A.

Fig. 6 shows that variations of $n(H_2)$ across the assumed range can produce changes in the $N(CH_3OH)/N(CO)$ ratios by a factor of 10, but that the increase depends only weakly on $n(H_2)$, as is expected when emission is thermalized and optically thin. The same exercise can be done for CH_3OH versus H_2O and the RADEX results are presented in Fig. 7. Because H_2O excitation is subthermal, the effect of $n(H_2)$ on this ratio is stronger than for CH_3OH versus CO. The resulting systematic variation in this case is ±1 order of magnitude and varies linearly with density.

4.2 Molecular column density ratios

With the appropriate range in physical conditions established, we are ready to address our original questions by exploring how the observed line intensity ratios convert into column density ratios. We start by examining the CH_3OH/CO column density ratio in order to quantify how much CH_3OH from the grains reaches the gas phase intact. Secondly, we examine the CH_3OH/H_2O ratio. All assumed

Table 2. Source properties.

Source	D (pc)	Coordinates α_{J2000}	δ_{J2000}	v_{LSR}[a] (km s^{-1})	L_{bol}[b] ($L_\odot$)	T_{bol}[b] (K)	M_{env}[c] ($M_\odot$)
NGC 1333 IRAS 2A	235	$03^h28^m55\overset{s}{.}60$	$+31°14'37\overset{''}{.}1$	+7.7	35.7	50	5.1
NGC 1333 IRAS 4A	235	$03^h29^m10\overset{s}{.}50$	$+31°13'30\overset{''}{.}9$	+7.2	9.1	33	5.2
NGC 1333 IRAS 4B	235	$03^h29^m12\overset{s}{.}00$	$+31°13'08\overset{''}{.}1$	+7.1	4.4	28	3.0

[a]Obtained from ground-based $C^{18}O$ or $C^{17}O$ observations (Yıldız et al. 2013) with the exception of IRAS 4A for which the value from Kristensen et al. (2012) is more consistent with our data.
[b]Measured using *Herschel*-PACS data from the WISH key programme (Karska et al. 2013).
[c]Mass within the 10 Kelvin radius, determined by Kristensen et al. (2012) from DUSTY modelling of the sources.

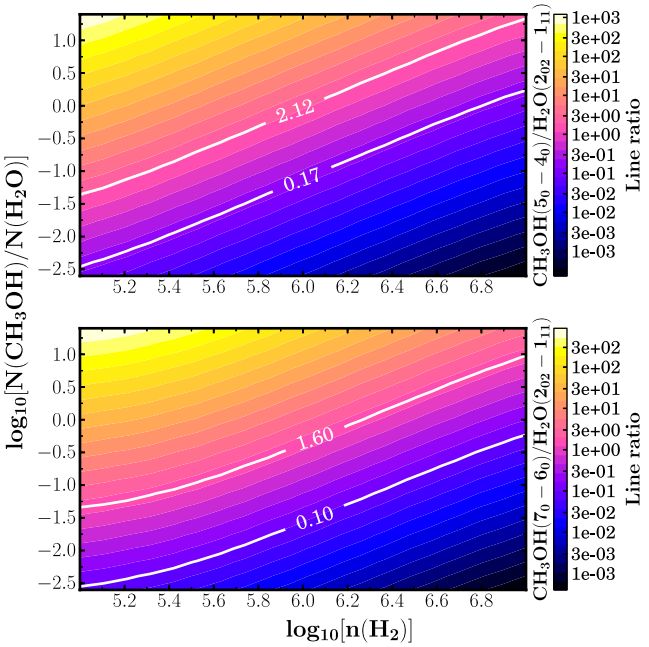

Figure 7. As Fig. 6, but for CH_3OH versus H_2O. T_{kin} is fixed at 200 K for both species.

Table 3. Physical conditions in the RADEX simulations.

Parameter	Value	Range	Effect
$\tau(H_2O)$	Optically thin[a]	0–20	<0.1 dex
T_{kin}	200 K	100–300 K	0.5 dex
$n(H_2)$	10^6 cm^{-3}	10^5–10^7 cm^{-3}	1.0-1.5 dex[b]

[a]The H_2O emission is optically thick but effectively thin (see text and Snell et al. 2000).
[b]$n(H_2)$ has a greater effect on $N(CH_3OH)/N(H_2O)$ than on $N(CH_3OH)/N(CO)$.

Table 4. Column density ratio ranges from the lowest (3 km s^{-1}) to highest velocities (10–18 km s^{-1}, depending on source).[a]

Source	$N(CH_3OH)/N(CO)$		$N(CH_3OH)/N(H_2O)$	
	3 km s^{-1}	max(v)	3 km s^{-1}	max(v)
IRAS 2A – blue	–	–	2(−1)	2(−1)
IRAS 2A – red	1(−2)	1(−2)	2(−1)	2(−1)
IRAS 4A – blue	3(−2)	3(−3)	1(0)	8(−2)
IRAS 4A – red	5(−3)	3(−3)	3(−1)	8(−2)
IRAS 4B – blue	1(−2)	4(−3)	2(−1)	3(−2)
IRAS 4B – red	8(−3)	3(−3)	1(−1)	2(−2)

[a]$a(b) = a \times 10^b$.

excitation conditions are listed in Table 3 and the resulting column density ratios are summarized in Table 4. The excitation conditions are assumed to be constant as a function of velocity. In order to convert N(p-H_2O) into $N(H_2O)$, we have assumed a constant ortho-to-para ratio of 3:1 and thus multiplied all calculated p-H_2O column densities by 4.

The CH_3OH/CO column density ratios are presented in the middle row of Fig. 8. Because the line wing emission is assumed optically thin, the column density ratio is proportional to the line ratio. With this assumption, we derive a CH_3OH/CO column density ratio that decreases with increasing velocity towards all sources by up to a factor of 5 (IRAS 4A blue). The CH_3OH/CO column density ratio is on average $\sim 10^{-3}$. We follow the example of Yıldız et al. (2013) and assume a CO/H_2 abundance of 10^{-4}. This value may be too high by a factor of a few (Dionatos et al. 2013; Santangelo et al. 2013), or too low by a factor of a few (Lacy et al. 1994). When using this CO abundance, the derived CH_3OH abundance becomes of the order of 10^{-7}, consistent with what is observed towards other outflows (e.g. Bachiller et al. 1995; Tafalla et al. 2010).

The CH_3OH/H_2O column density ratio decreases with increasing velocity offset, except towards IRAS 2A (Fig. 8, top row). The average column density ratio for all objects is $\sim 10^{-1}$. The $N(CH_3OH)/N(H_2O)$ ratios calculated using the two different emission lines of CH_3OH are noticeably different in the case of the red wing of IRAS 4A, by about a factor of 3, but the two lines show the same trend. Up until 10 km s^{-1}, the decrease in CH_3OH column density with respect to both CO and H_2O match each other closely and this is also reflected in the H_2O abundance being close to constant when compared to CO 10−9, as is seen in the middle row of Fig. 8. After 10 km s^{-1}, this behaviour changes especially towards the blue wing of IRAS 4A and possibly towards the red wing of IRAS 4B as well, with $N(CH_3OH)/N(H_2O)$ decreasing slightly more rapidly than $N(CH_3OH)/N(CO)$. The effect is also seen in $N(H_2O)/N(CO)$ which begins increasing at velocities above 10 km s^{-1}.

5 DISCUSSION

5.1 Velocity structure and the origin of the line emission

The protostellar wind and jet interact with the envelope in several locations:

(1) the stellar wind around the highly collimated bipolar jet;
(2) the shocked material where the stellar winds collide with the outflow cavity walls;
(3) the entrained material of the envelope, swept up but not necessarily shocked by the deflected stellar wind material.

These are illustrated in the left part of Fig. 9.

The last two of these are the environments most relevant to our study. In a scenario reminiscent of bow shocks (Smith, Khanzadyan & Davis 2003, also illustrated by middle part of Fig. 9), the point of impact between the stellar wind and outflow cavity walls will be dissociative and the shock will be J-type. The stellar wind colliding with the envelope material also becomes deflected by the cavity walls and sweeps up the surface layers in an entrained flow. The emission from the entrained flow is what is traced by different velocity components of the observed spectra, and these components are what we refer to for the remainder of the paper when discussing velocities. In the absence of other dissociating sources such as UV fields, the J-shock typically takes place at velocities of ∼25–30 km s^{-1} (Flower et al. 2003; Lesaffre et al. 2013). Beyond this we see no line emission in any of the sources included in this study. Further removed from the impact point, the post-shock gas has had time to cool down and molecules have had a chance to reform, while at the same time fresh molecular material from the envelope is being exposed to lower velocity (secondary) shocks originating in the bow wings of the original shock. Depending on the local magnetic field geometry, these shocks may be C-type or non-dissociative J-type (C-J-type) shocks. In our observations, this corresponds to line emission at velocities greater than a few km s^{-1}: the line wings at the lowest velocities (∼3–15 km s^{-1}) probe the entrained envelope material as well as secondary shocks and at higher velocities ($\gtrsim$15 km s^{-1}) they probe the directly shocked

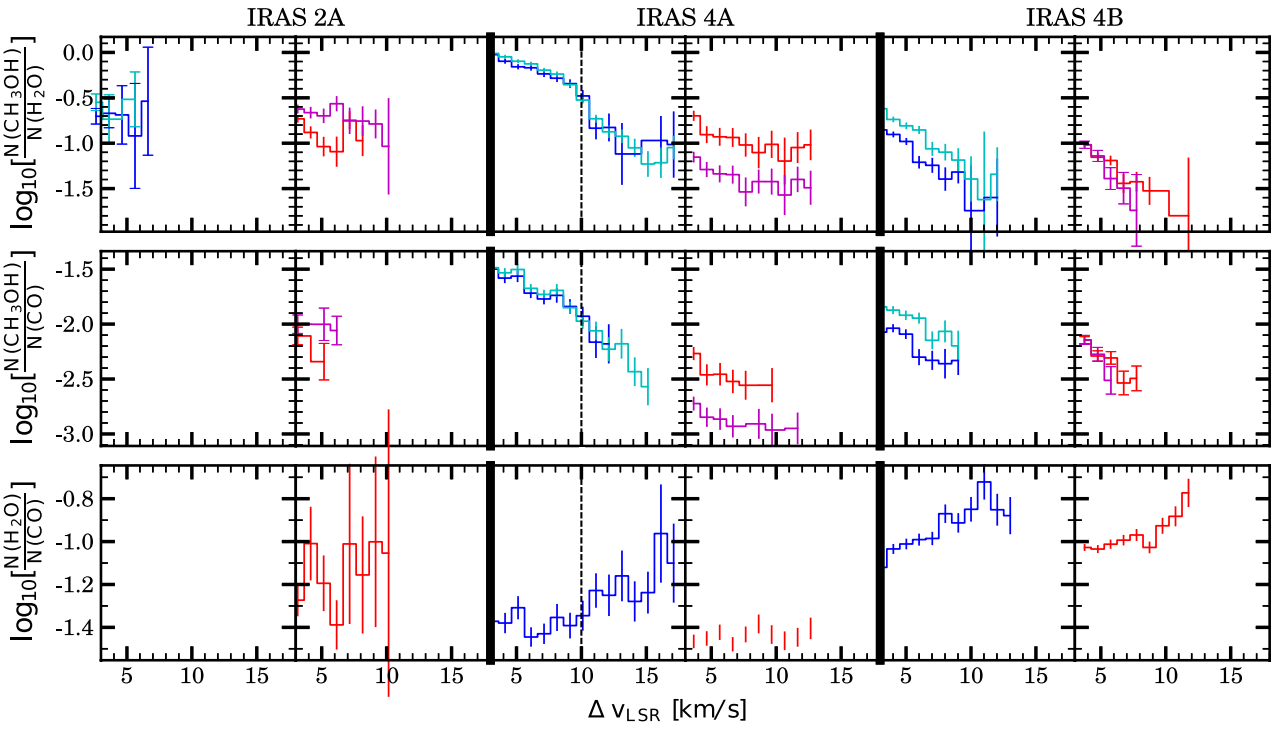

Figure 8. Line intensity ratios converted to corresponding column density ratios using the physical parameters presented in Table 3. The two top rows have had their ratios calculated using both the 5_0-4_0 (red and blue) and 7_0-6_0 (cyan and magenta) lines of CH_3OH. The dashed line at $\Delta v_{LSR} \approx 10\,km\,s^{-1}$ in the plots of the blue wing of IRAS 4A represents the approximate velocity where we see a change (compared to lower velocities) in the behaviour of $N(CH_3OH)/N(H_2O)$ and $N(H_2O)/N(CO)$. The line intensity ratios from which the column density ratios of the bottom row are calculated have been presented in Yıldız et al. (2013). Velocity is given with respect to the source velocity.

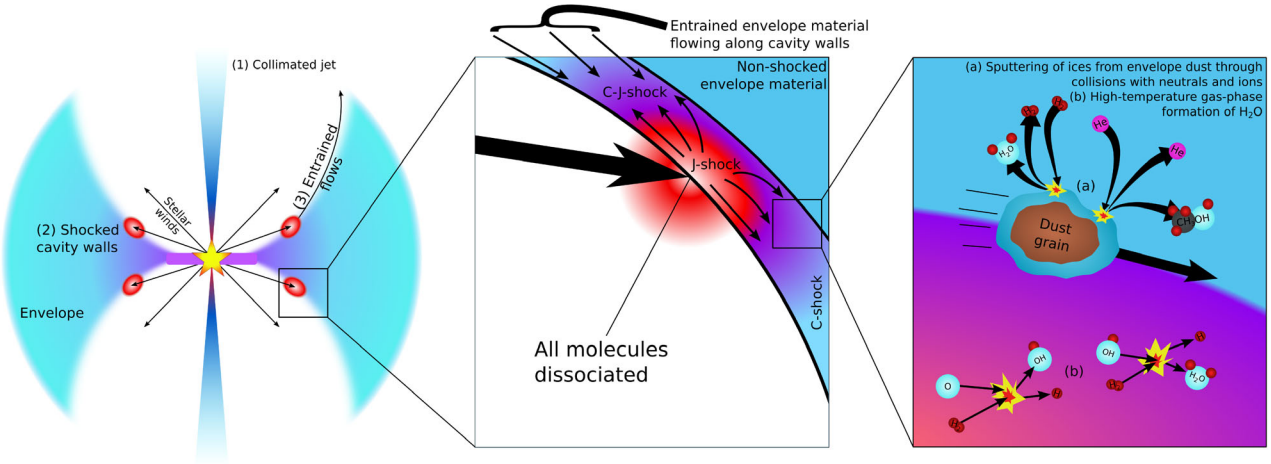

Figure 9. A cartoon (not to scale) illustrating the flow of material in the outflow regions of a YSO. The left part shows an overview of the region around the YSO, with the protostar and its protoplanetary disc in the middle of the envelope. A closer view of one of the shocked regions is illustrated in the middle part. The large arrow represents a maximum point of impact of the stellar wind on the envelope material, where the wind creates a very high temperature (several 10^4 K) J-type shock which causes the dissociation of all affected molecules. Further away from the impact point a C-J-type shock (non-steady state shock) is created and even further away a stable C-type shock develops. In addition to the deflected material of the wind flowing along the cavity walls, material from the envelope is entrained and forced to flow along the direction of the deflected wind. The right figure shows the relevant chemical processes happening in the shocked material: (a) the sputtering of ices from grain surfaces by collisions with neutrals and ions and (b) the high-temperature gas-phase formation of water.

material. The lowest velocity material ($\lesssim$3 km s^{-1}) is only related to the quiescent envelope, and is ignored in our analysis.

The physical conditions prevailing in the shocked regions and entrained flows enable a number of chemical and physical processes to happen, two of which are especially relevant to our study and are illustrated in the right part of Fig. 9. The sputtering effects (a) are relevant in entrained material where the gas and dust are not utterly destroyed in the process (C-J and C-shocks). Water and methanol ice that is sputtered from dust grains is expected to be present in the gas phase in both C-J- and C-shocked regions, i.e. at velocities

Table 5. Approximate observed velocity ranges for the different physical and chemical processes.

Approx. v range	Physical process	Chemical process
$\sim$3–10 km s^{-1}	Secondary CJ and C shocks	CH_3OH and H_2O sputtered and partly destroyed during sputtering CH_3OH destruction > H_2O destruction
$\sim$10–25 km s^{-1}	Secondary CJ and C shocks	CH_3OH sputtered + partly destroyed during sputtering/through reactions with H H_2O sputtered, partly destroyed by sputtering but also reformed
$\sim$3–10 km s^{-1}	Secondary shocks entraining envelope material	Additional sputtering and associated destruction?
$\gtrsim$25 km s^{-1}	Dissociative shocks	CH_3OH and H_2O destroyed completely; only H_2O reforms and is offset in velocity by the shock

below $\sim$25 km s^{-1}. The gas-phase formation reaction of water (b) is expected to activate when sufficiently high temperatures are reached in the shocked regions, and these regions will have an excess of water compared to solid-phase abundances. This temperature threshold is met within the velocity range occupied by the C- and C-J-shocked regions and any velocity above the threshold region will potentially have water formation happening up until the velocities where the physical conditions become dissociative.

This translation of velocity components in the spectra into different physical regions in the shock outflow cavity (summarized in Table 5) provides us with a sufficient context for the rest of discussion, in which we look at the results of the previous sections to answer the two questions we asked at the beginning of this paper:

(i) How much, if any, methanol is being destroyed in the outflows?

(ii) Is high-temperature water formation taking place in the outflows?

5.2 Molecular destruction in outflows

In dissociative J-type shocks, reactions with H are the most efficient way to destroy CH_3OH and other grain products such as water and ammonia. The activation energy for methanol reacting with H ($\sim$2270–3070 K; Sander et al. 2011) is even lower than that of ammonia which has already been shown to be destroyed in post-shock gas (Viti et al. 2011). Destroying water in a similar manner is more inefficient because the activation energy is higher ($\sim 10^4$ K), but at shock velocities of 25–30 km s^{-1} the kinetic temperature is already $>2\times10^4$ K (McKee & Hollenbach 1980) and so H_2O will also collisionally dissociate. We can readily observe this difference in activation energies between CH_3OH and H_2O destruction by H (Fig. 1). We see that in all cases H_2O emission in the wings tapers off below the 1σ noise level at significantly higher velocities ($\Delta v_{\rm LSR} > 25$ km s^{-1}) than the CH_3OH emission, which drops below noise levels at approximately $\Delta v_{\rm LSR} = 10$ km s^{-1} in most cases. The exception to this is IRAS 4A, which still shows trace methanol emission at up to 18 km s^{-1} and water emission at approximately 35 km s^{-1}.

The gas-phase CH_3OH abundances derived from the middle row of Fig. 8 can be compared to the expected solid-phase CH_3OH abundances. If we assume that equal abundances of envelope CH_3OH originate from dust grains at both the low-velocity and high-velocity regimes, the comparison leads to the conclusion that, towards high velocities, some fraction of CH_3OH originating from grain surfaces (90–99 per cent) is missing in the gas phase. This CH_3OH is either not being sputtered from the grains or is being destroyed in the sputtering process or in the gas phase.

Sputtering occurs when a neutral species, typically H_2, H or He, collides with the ice mantle of a dust grain with enough kinetic energy to release the ice species into the gas phase. Sputtering at shock velocities down to 10 km s^{-1} pre-dominantly takes place in C-type shocks (Flower & Pineau des Forêts 2010), where the negatively charged dust grains stream past the neutral gas. At these velocities, the kinetic energy of each particle is of the order of 1 eV. Sputtering yields have been calculated theoretically, but not measured in the laboratory, although 1 eV is significantly higher than the desorption energy barrier of CH_3OH or H_2O (both below 0.5 eV; Fraser et al. 2001; Burke & Brown 2010). However, given the high kinetic energy, it is likely that at least some molecules could be destroyed, rather than simply being desorbed by the sputtering process. This is more likely for CH_3OH than H_2O, given that the gas-phase dissociation energy of CH_3OH to H + CH_2OH is around 4 eV compared to just over 5 eV for H + OH (Blanksby & Ellison 2003). Furthermore, strong evidence exists that dissociation barriers are lowered in the condensed phase (Woon 2002). However, these sputtering processes are occurring in the same regions where we also expect methanol destruction by high-temperature gas-phase reactions with hydrogen atoms. Consequently, although our observations cannot distinguish between the two processes, itis clear that as the methanol abundance drops in the line wings, the sputtered methanol is being destroyed more readily than the water.

5.3 Water formation in outflows

At the highest outflow velocities, higher than those where we observe any methanol emission, water is readily observed. As discussed in Section 5.2, any water at even higher velocities will be destroyed by the J-shock and this is suggested by the lack of detectable H_2O emission beyond $\sim$25–30 km s^{-1}. Though the water destroyed in the J-shock is expected to eventually re-form via the high-temperature gas-phase route, the velocity of the re-formed water has been shifted to only be observable in the 'offset' component directly tracing the shock itself. This component has been removed in the decomposition of the H_2O spectra used in this analysis and has been separately discussed in Kristensen et al. (2013). The water at below J-shock velocities must have formed through gas-phase synthesis directly in the warm shocked gas. In our data, the column density ratio of H_2O/CO starts increasing at velocities higher than $\sim$10 km s^{-1} with respect to the source velocity. We conclude that the shift between water release from the grains and gas-phase water synthesis switches on at this velocity, since the water abundance remains constant with respect to CO (Yıldız et al. 2013) and CO is not destroyed unless the shocks have significantly higher velocities ($\sim$80 km s^{-1}; Neufeld & Dalgarno 1989). This is especially apparent in the blue wing of IRAS 4A and the red wing of IRAS 4B; the water abundance increases by a factor of $\sim$2, due to gas-phase formation. Below $\sim$10 km s^{-1}, our data show that the water abundance remains constant with respect to CO and we interpret this to indicate gas-phase water (and methanol) at low velocities which originated entirely from sputtered ice. There are two possibilities

for this low-velocity component: (i) if we consider the outflows to be conical shells (e.g. Cabrit & Bertout 1986, 1990), then a part of the cone, when projected on to the plane of the sky, will have a radial velocity component close to zero even if the 3D velocity in the cone is not zero anywhere; (ii) the post-shock or entrained material has decelerated and cooled down but has not had time to freeze out yet (Bergin, Neufeld & Melnick 1998). A combination of both possibilities may naturally also be at play. Observations at higher angular resolution are required to break this degeneracy by pinpointing where the emission from the lower velocity line wings originate spatially: inside the outflow cavity (option 1) or closer to the envelope (option 2).

6 CONCLUSIONS

We combined observations of H_2O, CH_3OH and CO line emission with RADEX simulations to constrain the gas-phase abundance variations of water and methanol towards three low-mass YSOs: IRAS 2A, IRAS 4A and IRAS 4B. We find that:

(i) The CH_3OH/CO column density ratio decreases by up to one order of magnitude with increasing velocity.

(ii) The abundance of CH_3OH in the shocked gas is more than 90 per cent lower than that reported for CH_3OH ice in the cold envelope. Given that the CO abundance is unaffected by shock chemistry across the velocity range investigated, this implies that CH_3OH is destroyed either during the ice sputtering process from dust grains or through gas-phase reactions with H in the outflow.

(iii) The H_2O/CO column density ratios increase by ∼a factor of 2, with the increase beginning at velocities above ∼10 km s^{-1}. This suggests that the gas-phase formation of water is active and significant at velocities higher than 10 km s^{-1}. No discontinuity is observed in the water column density as a function of velocity, implying that the transition is smooth and continuous between the observed water originating from ice sputtering and gas-phase routes.

(iv) The column density ratio of CH_3OH/H_2O also decreases with increasing velocity, closely matching the same trend in CH_3OH/CO column density ratio. Based on our prior conclusions, this implies that both H_2O and CH_3OH are sputtered from ices in these shocks, but that only CH_3OH is being destroyed, and no gas-phase H_2O formation is occurring, at least at velocities below 10 km s^{-1}.

(v) In the blue wing of IRAS 4A, the CH_3OH/H_2O column density ratio decreases more steeply at velocities in excess of ∼10 km s^{-1} than the CH_3OH/CO column density ratio. This traces the high-temperature gas-phase formation of water in this higher velocity regime.

Consequently, gas-phase CH_3OH and H_2O abundances in shocked regions depend on the complex interplay between ice sputtering mechanisms, gas-phase destruction processes and high-temperature formation reactions. These conclusions hint towards future observational and experimental requirements to further constrain the physics and chemistry of H_2O and CH_3OH in outflows. In particular, trying to observe and quantify the efficiency of CH_3OH and H_2O ice sputtering by neutrals in a laboratory environment would contribute towards verifying and/or refuting two of our main conclusions: whether or not the two molecules are sputtered with equal efficiency and if CH_3OH can be destroyed in the sputtering processes. Observations resolving the outflow spatially close to the protostar, and mapping the variation of physical conditions, are also important to further constrain these results.

ACKNOWLEDGEMENTS

ANS acknowledges financial support by the European Community FP7-ITN Marie-Curie Programme (grant agreement 238258). Astrochemistry in Leiden is supported by the Netherlands Research School for Astronomy (NOVA) by a Spinoza grant and by the European Community's Seventh Framework Programme FP7/2007-2013 under grant agreement 238258 (LASSIE). HIFI has been designed and built by a consortium of institutes and university departments from across Europe, Canada and the United States under the leadership of SRON Netherlands Institute for Space Research, Groningen, the Netherlands and with major contributions from Germany, France and the US. Consortium members are: Canada: CSA, Univ. Waterloo; France: CESR, LAB, LERMA, IRAM; Germany: KOSMA, MPIfR, MPS; Ireland, NUI Maynooth; Italy: ASI, IFSI-INAF, Osservatorio Astrofisico di Arcetri- INAF; the Netherlands: SRON, TUD; Poland: CAMK, CBK; Spain: Observatorio Astronomico Nacional (IGN), Centro de Astrobiologia (CSIC-INTA). Sweden: Chalmers University of Technology – MC2, RSS & GARD; Onsala Space Observatory; Swedish National Space Board, Stockholm University – Stockholm Observatory; Switzerland: ETH Zurich, FHNW; USA: Caltech, JPL, NHSC. The authors thank the referee for their helpful comments and questions.

REFERENCES

Bachiller R., Liechti S., Walmsley C. M., Colomer F., 1995, A&A, 295, L51
Bergin E. A., Neufeld D. A., Melnick G. J., 1998, ApJ, 499, 777
Bergin E. A., Neufeld D. A., Melnick G. J., 1999, ApJ, 510, L145
Bjerkeli P. et al., 2012, A&A, 546, A29
Blanksby S. J., Ellison G. B., 2003, Acc. Chem. Res., 36, 25
Boogert A. C. A. et al., 2008, ApJ, 678, 985
Brown W. A., Bolina A. S., 2007, MNRAS, 374, 1006
Burke D. J., Brown W. A., 2010, Phys. Chem. Chem. Phys., 12, 5947
Cabrit S., Bertout C., 1986, ApJ, 307, 313
Cabrit S., Bertout C., 1990, ApJ, 348, 530
Caselli P. et al., 2012, ApJ, 759, L37
Charnley S. B., 1999, in Greenberg J. M., Li A., eds, NATO ASIC Proc. 523: Formation and Evolution of Solids in Space. Kluwer, Dordrecht, p. 131
Codella C. et al., 2010, A&A, 518, L112
Cuppen H. M., van Dishoeck E. F., Herbst E., Tielens A. G. G. M., 2009, A&A, 508, 275
Daniel F., Dubernet M.-L., Grosjean A., 2011, A&A, 536, A76
Dartois E., Schutte W., Geballe T. R., Demyk K., Ehrenfreund P., D'Hendecourt L., 1999, A&A, 342, L32
de Graauw T. et al., 2010, A&A, 518, L6
Dionatos O., Jørgensen J. K., Green J. D., Herczeg G. J., Evans N. J., Kristensen L. E., Lindberg J. E., van Dishoeck E. F., 2013, A&A, 558, A88
Draine B. T., Roberge W. G., Dalgarno A., 1983, ApJ, 264, 485
Emprechtinger M. et al., 2013, ApJ, 765, 61
Flower D. R., Pineau des Forêts G., 2010, MNRAS, 406, 1745
Flower D. R., Le Bourlot J., Pineau des Forêts G., Cabrit S., 2003, MNRAS, 341, 70
Fraser H. J., Collings M. P., McCoustra M. R. S., Williams D. A., 2001, MNRAS, 327, 1165
Garrod R., Hee Park I., Caselli P., Herbst E., 2006, Faraday Discuss., 133, 51
Geppert W. D. et al., 2006, Faraday Discuss., 133, 177
Gibb E. L., Whittet D. C. B., Boogert A. C. A., Tielens A. G. G. M., 2004, ApJS, 151, 35
Glassgold A. E., Meijerink R., Najita J. R., 2009, ApJ, 701, 142
Green J. D. et al., 2013, ApJ, 770, 123
Herczeg G. J. et al., 2012, A&A, 540, A84
Herpin F. et al., 2012, A&A, 542, A76

Ioppolo S., Cuppen H. M., Romanzin C., van Dishoeck E. F., Linnartz H., 2008, ApJ, 686, 1474
Karska A. et al., 2013, A&A, 552, A141
Kristensen L. E., van Dishoeck E. F., van Kempen T. A., Cuppen H. M., Brinch C., Jørgensen J. K., Hogerheijde M. R., 2010a, A&A, 516, A57
Kristensen L. E. et al., 2010b, A&A, 521, L30
Kristensen L. E., van Dishoeck E. F., Tafalla M., Bachiller R., Nisini B., Liseau R., Yıldız U. A., 2011, A&A, 531, L1
Kristensen L. E. et al., 2012, A&A, 542, A8
Kristensen L. E., van Dishoeck E. F., Benz A. O., Bruderer S., Visser R., Wampfler S. F., 2013, A&A, 557, A23
Lacy J. H., Knacke R., Geballe T. R., Tokunaga A. T., 1994, ApJ, 428, L69
Lamberts T., Cuppen H. M., Ioppolo S., Linnartz H., 2013, Phys. Chem. Chem. Phys., 15, 8287
Lee H.-H., Bettens R. P. A., Herbst E., 1996, A&AS, 119, 111
Lesaffre P., Pineau des Forêts G., Godard B., Guillard P., Boulanger F., Falgarone E., 2013, A&A, 550, A106
McKee C. F., Hollenbach D. J., 1980, ARA&A, 18, 219
Manoj P. et al., 2013, ApJ, 763, 83
Maret S., Ceccarelli C., Tielens A. G. G. M., Caux E., Lefloch B., Faure A., Castets A., Flower D. R., 2005, A&A, 442, 527
Mottram J. C., van Dishoeck E. F., Schmalzl M., Kristensen L. E., Visser R., Hogerheijde M. R., Bruderer S., 2013, A&A, 558, A126
Neufeld D. A., Dalgarno A., 1989, ApJ, 340, 869
Nisini B. et al., 2010, A&A, 518, L120
Nisini B. et al., 2013, A&A, 549, A16
Öberg K. I., Boogert A. C. A., Pontoppidan K. M., van den Broek S., van Dishoeck E. F., Bottinelli S., Blake G. A., Evans N. J., 2011, ApJ, 740, 109
Pickett H. M., Poynter R. L., Cohen E. A., Delitsky M. L., Pearson J. C., Muller H. S. P., 1998, J. Quant. Spectrosc. Radiat. Transfer, 60, 883
Pilbratt G. L. et al., 2010, A&A, 518, L1
Pontoppidan K. M., Dartois E., van Dishoeck E. F., Thi W.-F., D'Hendecourt L., 2003, A&A, 404, L17
Pontoppidan K. M., van Dishoeck E. F., Dartois E., 2004, A&A, 426, 925
Rabli D., Flower D. R., 2010, MNRAS, 406, 95
Roelfsema P. R. et al., 2011, A&A, 537, A17
Sander S. et al., 2011, Chemical Kinetics and Photochemical Data for Use in Atmospheric Studies, Evaluation No. 17 JPL Publication 10-6, Jet Propulsion Laboratory, Pasadena, CA, available at: http://jpldataeval.jpl.nasa.gov
Santangelo G. et al., 2012, A&A, 538, A45
Santangelo G. et al., 2013, A&A, 557, A22
Schöier F. L., van der Tak F. F. S., van Dishoeck E. F., Black J. H., 2005, A&A, 432, 369
Smith M. D., Khanzadyan T., Davis C. J., 2003, MNRAS, 339, 524
Snell R. L. et al., 2000, ApJ, 539, L93
Tafalla M., Santiago-Garcia J., Hacar A., Bachiller R., 2010, A&A, 522, A91
Tafalla M. et al., 2013, A&A, 551, A116
Tielens A. G. G. M., 2005, The Physics and Chemistry of the Interstellar Medium. Cambridge Univ. Press, Cambridge
Tielens A. G. G. M., Hagen W., 1982, A&A, 114, 245
van der Tak F. F. S., van Dishoeck E. F., Caselli P., 2000, A&A, 361, 327
van der Tak F. F. S., Black J. H., Schoier F. L., Jansen D. J., van Dishoeck E. F., 2007, A&A, 468, 627
van Dishoeck E. F. et al., 2011, PASP, 123, 138
Van Loo S., Ashmore I., Caselli P., Falle S. A. E. G., Hartquist T. W., 2013, MNRAS, 428, 381
Vasta M. et al., 2012, A&A, 537, A98
Visser R., van Dishoeck E. F., Doty S. D., Dullemond C. P., 2009, A&A, 495, 881
Viti S., Jimenez-Serra I., Yates J. A., Codella C., Vasta M., Caselli P., Lefloch B., Ceccarelli C., 2011, ApJ, 740, L3
Woon D. E., 2002, Int. J. Quantum Chem., 88, 226
Yang B., Stancil P. C., Balakrishnan N., Forrey R. C., 2010, ApJ, 718, 1062
Yıldız U. A. et al., 2013, A&A, 556, 48

APPENDIX A: CORRECTING FOR DIFFERENTIAL BEAM DILUTION

As seen in Table 1, the lines that are examined in this study have somewhat different beam sizes from each other, ranging from 11 arcsec with the CH_3OH $5_K - 4_K$ lines to 22 arcsec with the H_2O $2_{02} - 1_{11}$ line. These variations in beam size lead to large variations from line to line in the beam dilution of the observed emission, which has to be compensated for if we are to make an accurate comparison between the different lines. To do this, we have applied to our line ratios – discussed in Sections 3.2 and 4.2 – the differential beam dilution correction method detailed in appendix B of Tafalla et al. (2010).

The correction method is applied by assuming a simple Gaussian beam, where the beam dilution factor is proportional to $\theta_{\rm MB}^{-\alpha}$, where $\theta_{\rm MB}$ is the full width at half-maximum of the beam being examined and α is a free parameter dependant on the source size and which can vary between 0 and 2. Tafalla notes that $\alpha = 2.0$ for a point-like source, 1.0 for a one-dimensional source and 0.0 for a source infinitely extended in two dimensions. For our case, in applying a beam dilution correction to an observed line intensity ratio $T_{\rm R,\,1}/T_{\rm R,\,2}$ between molecules 1 and 2 can be done using the equation

$$(T_{\rm R,1}/T_{\rm R,2})_{\rm corrected} = (T_{\rm R,1}/T_{\rm R,2})(\theta_{\rm MB,2}/\theta_{\rm MB,1})^{-\alpha}. \quad \text{(A1)}$$

In order to apply this correction method to our data, we had to first examine which value of α is most appropriate to our case. The effect of accounting for beam dilution, or lack thereof, in our case is best seen when translating the line ratio of the two different CH_3OH lines against either of the CO lines or the H_2O line we have studied in this paper. For the case of finding out α, we decided to use the CO (10–9) line because of the three non-CH_3OH lines it is the one least affected by high optical depth. Using the assumption that emission from both of the CH_3OH lines' wings originate from the same physical region of the YSO, we would expect that when beam dilution is taken into account correctly, the line ratios of both CH_3OH lines divided by the CO (10–9) would yield the same N(CH_3OH)/N(CO).

We decided to adopt $\alpha = 1.0$ as the beam-size correction exponent for all our cases. According to Tafalla et al. (2010), this implies that the emission we are probing is extended along one dimension when compared to our beam sizes.

APPENDIX B: ROTATIONAL DIAGRAMS FOR CH_3OH

We see emission from several transitions in both A-CH_3OH and A-CH_3OH. Though most of the lines are very weak and/or

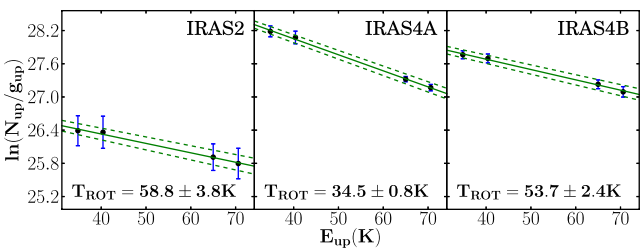

Figure B1. Rotational diagrams of CH_3OH for the integrated intensity of both wings in IRAS 2A (left), IRAS 4A (middle) and IRAS 4B (right). The solid green line is the linear fit to the shown points and the dashed green lines show the uncertainty range of the fit as determined by the 1σ uncertainties of the fit parameters.

blended with each other, we can use the four strongest lines (A-$CH_3OH(5_0-4_0)$, A -$CH_3OH(7_0-7_0)$, E -$CH_3OH(5_{-1}-4_{-1})$ and E -$CH_3OH(7_{-1}-7_{-1})$) to construct rotational diagrams, which are presented in Fig. B1 for all three objects. We calculate $T_{\rm rot} = 57.8 \pm 4.3$ K for IRAS 2A, 34.6 ± 1.3 K for IRAS 4A and 53.7 ± 2.0 K for IRAS 4B. It is also possible to construct rotational diagrams separately for the red and blue wings of the three objects. In doing so, one ends up with $T_{\rm rot,\,red} = 91.5 \pm 32.7$ K and $T_{\rm rot,\,blue} = 46.9 \pm 2.7$ K for IRAS 2A, $T_{\rm rot,\,red} = 23.4 \pm 2.2$ K and $T_{\rm rot,\,blue} = 40.8 \pm 2.4$ K for IRAS 4A and $T_{\rm rot,\,red} = 59.9 \pm 7.9$ K and $T_{\rm rot,\,blue} = 52.3 \pm 4.4$ K for IRAS 4B.

This paper has been typeset from a TEX/LATEX file prepared by the author.